

# Parameter-free prediction of irradiation defect structures in tungsten at room temperature using stochastic cluster dynamics

Sicong He<sup>1</sup>, Brandon Schwendeman<sup>2</sup>, George Tynan<sup>2</sup>, Jaime Marian<sup>1,3</sup>

<sup>1</sup>Department of Materials Science and Engineering, University of California Los Angeles, Los Angeles, CA 90095, USA

<sup>2</sup>Department of Mechanical and Aerospace Engineering, University of California San Diego, La Jolla, CA 92093, USA

<sup>3</sup>Department of Mechanical and Aerospace Engineering, University of California Los Angeles, Los Angeles, CA 90095, USA  
E-mail: jmarian@ucla.edu

December 23, 2025

## Abstract

The foundations of irradiation damage theory were laid in the 1950s and 60s within the framework of chemical reaction kinetics. While helpful to analyze qualitative aspects of irradiation damage, the theory contained gaps that delayed its implementation and applicability as a predictive tool. The advent of computer simulations with atomistic resolution in the 80s and 90s revealed a series of mechanisms that have proved essential to understand key aspects of irradiation damage in crystalline solids. However, we still lack a comprehensive model that can connect atomic-level defect physics with experimental measurements of quantitative features of the irradiated microstructure. In this work we present a mesoscale model that draws from our improved understanding of irradiation damage processes collected over the last few decades, bridging knowledge gained from our most sophisticated atomistic simulations with defect kinetics taking place over time scales many orders of magnitude larger than atomic interaction times. Importantly, the model contains no adjustable parameters, and combines several essential pieces of irradiation damage physics, each playing an irreplaceable role in the context of the full model, but of limited utility if considered in isolation. Crucially, we carry out a set of experiments carefully designed to isolate the key irradiation damage variables and facilitate validation. Using tungsten as a model material, we find exceptionally good agreement between our numerical predictions and experimental measurements of defect densities and defect cluster sizes.

## 1 Introduction

The study of irradiation damage and its accumulation and effects on material properties is an exceedingly complex problem that has attracted considerable attention over the last several decades [1, 2, 3, 4, 5, 6, 7]. Irradiation brings the system to a far-from-equilibrium state generally characterized by defect concentrations many orders of magnitude higher than in thermal conditions. This triggers a number of transformations that lead to *microstructural evolution*, understood as a series of processes by which the system changes its internal structure to reduce its defect concentrations and lower its free energy.

A popular choice in the study of irradiation damage in metals is tungsten (W), which has attracted substantial attention in recent times as a candidate plasma-facing material in fusion energy devices [8, 9, 10, 11, 12, 13]. As such, considerable effort has been put on developing material models that can capture the fine-scale features of irradiation damage in W. Electronic structure calculations based on density functional theory (DFT) are typically employed to calculate fundamental material properties and defect energetics [14, 15, 16, 17], while classical molecular dynamics (MD) simulations are used to obtain transport properties and simulate collisional displacement events [18, 19, 20, 21]. However, while atomistic simulations provide high physical accuracy, they do so at the expense of computational efficiency, eliminating them as a viable tool to reach irradiation doses of interest in experimental studies. Instead, simulations of high-dose irradiation in pure W are done using ‘object’ kinetic Monte Carlo (okMC), or mean-field rate theory (MFRT) methods [14, 22, 23, 10, 24, 25, 26, 27, 28, 29, 30]. These methods make use of computationally or experimentally obtained defect properties to surge above atomic-level time dynamics and extend the simulations’ time reach into the dpa scale. Unfortunately, lacking a clear reference to benchmark against, these studies are hampered by the need to incorporate the large number of irradiation mechanisms that have been proposed for W [10]. Recent experiments have been carried out to fill this gap [31, 32, 33], providing much needed information about the defect species present in the microstructure as a function of key irradiation variables.

However, given the breadth and depth of irradiation effects in W that are captured in the models, it is of interest to carry out targeted experiments to isolate specific variables that may help us discriminate among the key mechanisms controlling the material response in each case. The main objective of this work is to perform a set of carefully designed irradiation experiments to help shed light on some of the most fundamental response mechanisms of irradiated W. We intentionally use tungsten specimens with minimum internal microstructure, i.e., well-annealed, very high-purity W single crystals with no dislocations or grain boundaries. With this choice, we eliminate the need to consider empirical bias factors for defect absorption by sinks, which are traditionally a source of confusion in many studies of irradiation damage modeling, particularly in metals [34, 35, 29]. Our simulations and experiments are conducted at 290 K, below irradiation recovery Stage III in W, where vacancy motion is negligible. All together, these conditions present a unique opportunity to validate specific aspects of the physical model of irradiation damage in W.

## 2 Physical model of irradiation damage

Mean-field rate theory provides the basis within which a system of partial differential equations (PDE) representing the coupled cluster dynamics can be solved to simulate the evolution of irradiation damage in materials [36, 37, 38]. Figure 1 shows the generalized mean-field cluster dynamics PDE based on classical nucleation theory. As the figure illustrates, the equation is formulated as a linear superposition of process change rates, truncated to second-order defect interactions to sim-

plify the many-body problem<sup>1</sup>. Numerical integration of this PDE system is feasible on modern computers, although to obtain practicable solutions, it is still necessary to apply certain numerical workarounds to accelerate the simulations [40, 41].

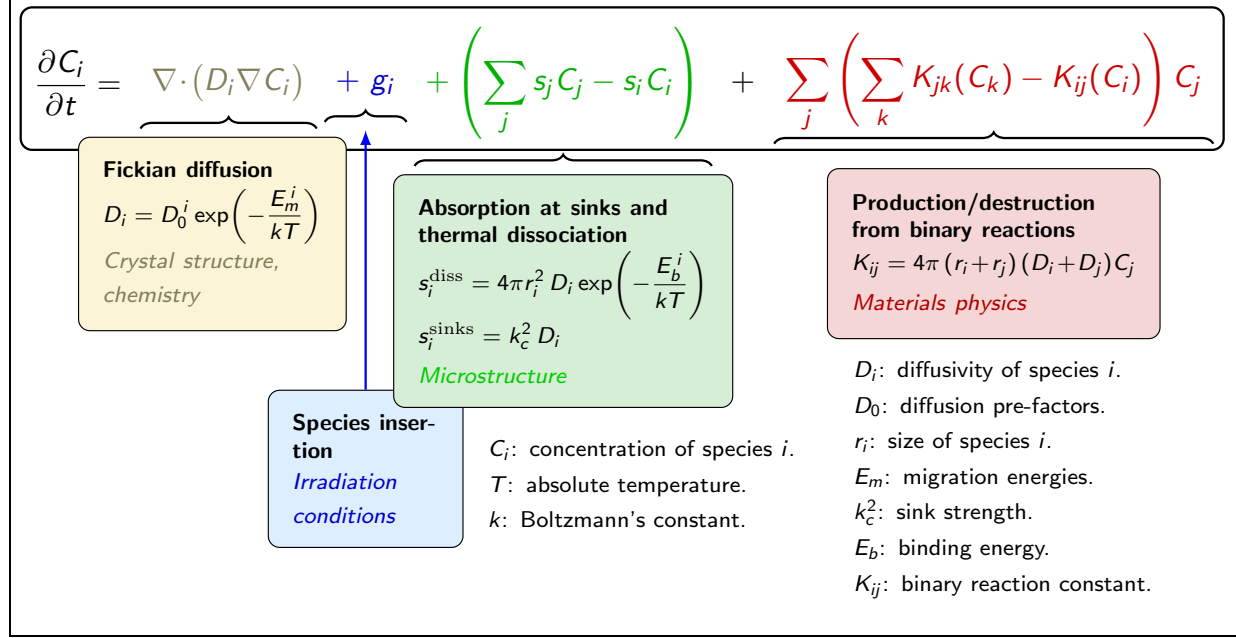


Figure 1: Generalized mean-field cluster dynamics PDE based on classical nucleation theory. The right-hand side of the equation is broken down into separate contributions representing fundamentally different physical processes. These include diffusion, insertion of damage species, thermal evaporation of monomers from clusters, defect absorption at system sinks, and second-order cluster reaction kinetics. Each term is defined by specific material coefficients. (diffusivities, dissolution probabilities, sink strengths, reaction constants, etc.). All these coefficients encode the physics of the process, the host material, and the microstructure. The expression for the reaction coefficient  $K_{ij}$  in the red box labeled *Materials Physics* represents the specific case of mutually-reacting 3D-moving objects.

Models such as this one are useful because they are formulated in a general and flexible manner intended to accommodate our latest knowledge in irradiation effects coming from a number of more accurate simulation methods. These may include (i) correlated defect distributions from displacement cascades, (ii) irradiation phenomena such as radiation enhanced diffusion, (iii) radiation induced precipitation and segregation, (iv) multi-species chemistry, etc. This information is generally encoded in coefficient matrices with the same dimensionality as that of the the PDE system. However, the above system of equations is designed to capture the entire defect cluster population from  $i = 1, \dots, N$ , where  $N$  is the largest cluster size, which can in some cases reach millions of point defects. As such, the dimensionality of the cluster population can be extremely large, making the solution of these systems a tremendous numerical challenge. This also means that the physical coefficient matrices can be very large, sparse in some regions of the cluster dimensional space, while concentrated in others, with elements that have widely disparate values, and which can be time-evolving. This represents a mathematical challenge that even the most formidable deterministic

<sup>1</sup>This is generally a very good approximation, as the interaction cross sections for three-body reactions and above are extremely small [39].

solvers can struggle with.

One can however solve the PDE system within the mean-field approximation by treating each term in the coefficient matrix as if it was an event rate. In this fashion, one naturally introduces the stochastic variability of explicit stochastic methods such as the kinetic Monte Carlo (kMC) approach but the mathematical form of MFRT methods is preserved. Event rates must be defined for a specific material volume, much like for kMC simulations, but matrix coefficients are obtained as for MFRT simulations. Likewise, spatial derivatives (diffusion terms) can be converted to rates in the simulation volume using the divergence theorem with standard discretizations as in the deterministic case. We call this method *stochastic cluster dynamics* (SCD) [42]. A brief review of SCD is provided in [A](#), and for the remainder of this paper, the SCD method should be considered a stochastic version of the MFRT method, identical in its theoretical basis but more versatile and flexible in terms of the domain of application of the model and the numerical robustness of its solutions.

## 2.1 Experimental

The experiments have been designed to prioritize validation and facilitate comparison with the model predictions. Specifically, experimental and simulation conditions are harmonized by taking into consideration the following points:

1. Material microstructure: the coefficients  $k_c^2$  shown in the second term in the r.h.s. of [Fig. 1](#), known as *sink strengths*, are difficult to calculate and subject to a large degree of empiricism [35]. Using well-annealed, high-purity single crystals avoids the presence of grain boundaries, dislocations, and precipitates, typically the most potent defect sinks found in crystalline materials.
2. Irradiation temperature: the irradiations were conducted at 290 K, which is below the Stage III temperature below which there is no vacancy mobility [43, 44]. This leaves single self-interstitial atoms (SIA) and di-interstitials as the sole mobile species in the system [45, 46, 43, 47, 48], which simplifies the kinetics in the simulations.
3. Irradiation with high-energy W self-ions ensures sufficient penetration to isolate the high-damage region of the specimen from its front and back surfaces, eliminating spurious local effects resulting from undue proximity of defects to the free surfaces. As well, implanting with W self-ions eliminates potential chemical interactions between the ions and the host lattice.

The experimental data were acquired using X-ray diffuse scattering (XRDS) [31], which can probe macroscopic volumes and thus isolate the irradiated samples from surface effects, as is often the case in TEM foils [49]. As well, XRDS provides a higher defect size sensitivity, resolving defects as small as 0.5 nm (tens of atoms, well below typical TEM resolution limits) and can distinguish between defect types, i.e., vacancies and self-interstitials and clusters thereof, adding an extra opportunity for comparison with defect evolution models. However, note that, due to resolution disparities, XRDS does not necessarily capture equal numbers of vacancies and self-interstitials in the clusters. This is again an opportunity for verification of the model predictions with respect to the experimental cluster concentrations.

## 2.2 Simulation conditions

Table 1: SCD simulation parameters defined from the experimental conditions in ref. [50].

Parameter	Symbol	Value	Units
Ion fluence	-	$2.34 \times 10^{12}$	$\text{cm}^{-2}$
Irradiation time	$\Delta t_{\text{irr}}$	93	s
Ion flux	-	$2.52 \times 10^{10}$	$\text{cm}^{-2} \cdot \text{s}^{-1}$
Total dose	-	0.008	dpa
Dose rate	$\dot{\gamma}$	$8.6 \times 10^{-5}$	$\text{dpa} \cdot \text{s}^{-1}$
Temperature	$T$	290	K
Atomic density	$\rho_a$	$6.3 \times 10^{28}$	$\text{m}^{-3}$
Burgers vector	$b$	0.27	nm
Numerical volume	$\Omega$	$10^{-18}$	$\text{m}^3$
Annealing time	-	3600	s

The starting point for simulating irradiation damage processes in crystals is the PKA (primary knock-on atom) energy distribution function, which describes the energies with which recoils are produced during irradiation. For ions, the PKA distribution is extracted from SRIM simulations in full cascade mode [51]. Figure 2 shows the cumulative PKA energy distribution functions,  $C(x; E)$ , for the experiments performed by Schwendeman et al. [31] in pure W. The SRIM calculations indicate that the energy expended on lattice damage out of the total 10.8 MeV of ion energy is 2.65 MeV. Additionally, the average number of displacements,  $N_{\text{NRT}}$ , per ion track was 18,373. The mean PKA energy can then be obtained from Fig. 2 as:

$$\langle E \rangle = \int_0^L \int_0^\infty C(x; E) \, dx \, dE \quad (1)$$

which reflects the depth dependence of recoil production in ion irradiation experiments through the variable  $x$ , extending from the front surface at  $x = 0$  to the back surface at  $x = L$ , as well as its dependence on energy  $E$ . For the present case, we obtain a value of  $\langle E \rangle = 0.8$  keV, although it is important to note, as we will demonstrate below, that  $\langle E \rangle$  is not a representative substitute of the full PKA energy spectrum. Damage accumulates at a rate of  $8.6 \times 10^{-5}$  dpa·s<sup>-1</sup><sup>2</sup>. These, and the rest of the simulation parameters are given in Table 1.

The simulations also include a one-hour annealing period at 290 K. This annealing is simulated by allowing the defects present in the system after irradiation to evolve according to their thermal relaxation laws (see terms with exponential terms in Fig. 1 and eq. (5)). Thermal annealing is generally controlled by diffusion of mobile species and dissociation of large immobile species by emission of monomers.

## 2.3 Key physics ingredients of the model

The model captures several crucial pieces of irradiation defect physics without which it would have not been possible to match experimental measurements. Some of these have only recently become available in the form of very recent works:

---

<sup>2</sup>We use the common unit of *displacements per atom* or ‘dpa’ to represent the damage fluence. In our experiments, 1 dpa amounts to a dose of approximately  $2.3 \times 10^{14}$  ions per  $\text{cm}^2$  [31].

Figure 2: Cumulative PKA energy distribution function as a function of ion penetration depth due to 10.8-MeV W ion irradiation in W. The dashed black line represents the depth at which the maximum damage is attained ( $x=600$  nm). The dashed red line indicates the depth damage profile at the point of saturation, which is seen to roughly follow a Bragg profile. The average PKA energy, obtained by integration of the two-dimensional surface in the entire  $x$ - $E$  space is 0.8 keV.

1. Using cascade defect distributions obtained directly from MD simulations, without accounting for post-cascade correlated recombination.
2. Using a universal fractal law for the sizes of defect clusters directly emerging from displacement cascades, regardless of whether they are of SIA or vacancy nature.
3. Assuming that the only mobile species are single self-interstitials, di-interstitials, and mono-vacancies.
4. Capturing the fast one-dimensional character of SIA diffusion at low temperature.
5. Considering sufficiently large simulation volumes to appropriately sample the recoil energy distribution's high energy tail.

Next, we discuss each one of these times in detail as they have been implemented in the model.

### 2.3.1 Defect production in high-energy displacement cascades

The quantity  $\tilde{g}$  in eq. (5) represents the insertion rate of defect species in the system. Defects are introduced in discrete bursts, each representing an independent displacement cascade, which are generated using correlations extracted from extensive databases obtained with molecular dynamics (MD) simulations of high-energy displacement cascades in W [52, 53, 54]. The information contained in these databases includes (i) the total number of Frenkel pairs,  $N_{\text{PKA}}$ , produced by a PKA with a given energy, (ii) the fraction of defects forming part of clusters, and (iii) the cluster size distribution. Here we use the following expressions

$$N_{\text{PKA}} = \begin{cases} 3.81E^{0.62}, & E \leq 48 \text{ keV} \\ 0.50E^{1.15}, & E > 48 \text{ keV} \end{cases} \quad (2)$$

These correlations are all dynamically sampled by the SCD code in every iteration and defects are introduced according to the PKA energy distribution provided in Fig. 2. Note that some of these works are very recent (and supersede previous studies [55, 56]) and thus only available to the nuclear materials community in the last few months.

### 2.3.2 Cluster size distribution

While the total number of Frenkel pairs per PKA is the starting point of the defect insertion process, another key piece of information concerns the sizes of the defect clusters inserted in the simulation volume with every displacement cascade. Detailed studies based on MD simulations have suggested that cluster sizes follow a universal scaling law independent of PKA energy [56, 26]. This is substantiated by recent results by Byggmastar et al. [54] including cascades with PKA energies up to 2 MeV. The normalized histograms based on the full dataset are shown in Figure 3 for vacancy, Fig. 3(a), and SIA, Fig. 3(b), clusters. We have fitted the distributions to inverse power laws with scaling  $\sim n^{-S}$ , where  $n$  is the number of point defects in the cluster and  $S$  is the scaling exponent. As the plots show, the exponents are  $-1.6$  and  $-1.9$  for vacancy and SIA clusters, denoted as  $I_n$  and  $V_n$ , respectively. We use these values in our simulations to allocate the number Frenkel pairs generated by each PKA using the damage correlations in eqs. (2) to defect clusters, until the total number of defects per cascade is fully apportioned.

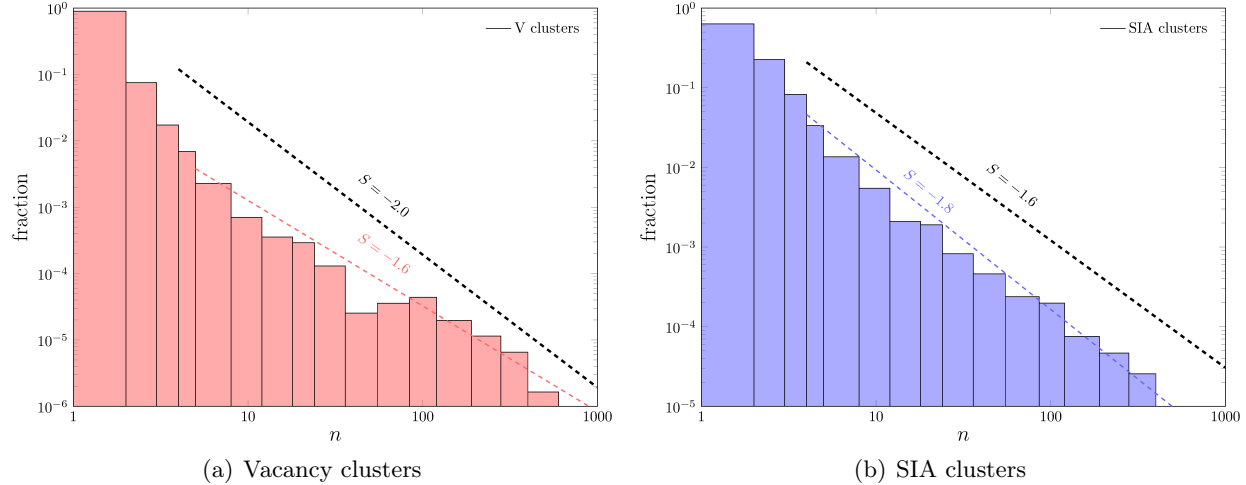


Figure 3: Cluster size distributions for W from high-energy displacement cascade simulations by Byggmästar et al. [54]. (a) Vacancy clusters. (b) SIA clusters. Inverse power law exponents are shown next to dashed segments, indicating the numerical scaling expected for cluster sizes above  $n > 4$ . The correlations extracted from the work of Sand et al. [56] are shown as black dashed lines for comparison.

### 2.3.3 Mobile defect species

As discussed above, the majority of defect clusters larger than a given size adopt a prismatic loop configuration. These loops are defined unequivocally by their Burgers vector and by their habit plane [57, 58]. While in principle all perfect (unfaulted) loops are glissile along their Burgers vector's direction, in W they are practically immobile for clusters with more than three interstitials or one vacancy [59]. Indeed, there is consistent evidence from isochronal annealing studies that the only species contributing to recovery in stages I, II, and III are, respectively, single SIA, di-interstitials, and monovacancies [45, 46, 60, 43, 47, 48, 44]. TEM experiments in high-purity electron irradiated W have shown that clusters move only in highly driven conditions, distinct from conventional ion beam irradiation conditions [61]. Even in atomistic simulations, in pure lattices with no impurities or imperfections, it has been shown that small SIA clusters have a reduced mobility compared to other BCC metals [62]. Object kinetic Monte Carlo simulations also point to limited or no SIA cluster mobility in W to find consistency with experimental defect concentration measurements [24].

Despite some contradicting work on the diffusion properties of single self-interstitials, in which migration energies as high as 0.3 eV have been proposed [15, 63, 64, 65], we have found that the migration energies of SIA that lead to agreement with the present experiments (and are consistent with additional experimental measurements [66] should be  $< 0.01$  eV. Indeed, one of the main reasons for these low SIA migration energies is that their migration is almost exclusively one-dimensional along  $\langle 111 \rangle$  directions [66]. It is known that considering rotation as part of the transport mechanism of SIA leads to larger effective migration energies, as several atomistic calculations have demonstrated [67, 15, 64, 68]. However, this is at odds with experimental observations [69, 66, 70] (and other conflicting atomistic studies [67, 14, 59]). As well, some authors have suggested that the reason for this low migration energies is that quantum effects may suppress the temperature dependence at low temperatures in W [71]. With that in mind, the diffusivity parameters for the mobile species in our model, and the source for their values, are as listed in Table 2.

Table 2: Diffusivity parameters for the mobile defects employed in this work.

Defect	$D_0$ [m $^2$ .s $^{-1}$ ]	$E_m$ [eV]	source
$I_1$	$8.77 \times 10^{-8}$	0.009	[59, 70]
$I_2$	$7.97 \times 10^{-8}$	0.024	[59]
$V_1$	$1.11 \times 10^{-6}$	1.71	[72, 17, 73, 70, 74]

## 2.4 One-dimensional migration of single self-interstitials

As indicated in the previous subsection, SIA mobility is a key property governing the agreement between the experimental measurements and the modeling predictions. With the migration properties firmly established, here we characterize its other crucial aspect: 1D diffusion<sup>3</sup>. Consideration of one-dimensional migration of self-interstitials implies employing material parameters in eq. (5) that reflect this characteristic of SIA motion. In particular, 1D migration leads to specific coefficients  $\tilde{s}_i$  and  $\tilde{k}_{ij}$ . In our setting, where the only operational defect sinks are free surfaces bounding the irradiated sample film, the corresponding sink strength,  $k_c^2$ , for SIA migration is [75, 76]:

$$k_c^2 = \frac{4}{l^2}$$

where  $l$  is the thickness of the irradiated film. The reaction rate between a 1D-moving species  $i$  (e.g., a single-interstitial) and an immobile object  $j$  (a vacancy, vacancy cluster, or another SIA cluster) is written as [76]:

$$K_{ij} = 8\pi D_i (r_i + r_j)^2 C_i C_j^{4/3} \quad (3)$$

where  $D_i$  is the diffusivity of (mobile) species  $i$ ,  $r_i$  and  $r_j$  are the interaction radii of the two reacting species, and  $C_i$  and  $C_j$  are their respective concentrations. Note that, for low values of  $C_j$ , the above rate closely resembles that of the 3D-3D case. After Huang and Marian [76], due to their extremely low interaction cross-section, the reaction rate between two one-dimensionally migrating species reactions (e.g., single SIA reacting with one another) is neglected in this work.

### 2.4.1 PKA energy distribution tail

The final element in our model that has a strong bearing on the ability of our simulations to capture the experimental size distributions is the need to introduce PKA with sufficiently-high energies to sample the large-size portion of the cluster size distribution. As justified above, due to the limited defect mobility at 290 K in W, the only feasible formation mechanism of large loops in this case is by direct injection in displacement cascades.

However, as noted by Sand et al. [56] and Byggmästar et al. [54], the probability of generating loops with more than 100 defects in W requires PKA energies higher than 100 keV. This is consistent with the expressions used in this work, given in eq. (2). From Fig. 2, the probability of sampling energies larger than 100 keV is one in 100,000. Our SRIM simulations indicate that each ion on average creates  $N_{\text{NRT}} = 18373$  recoils, i.e., a minimum of six ion insertions is needed to produce at least one 100-keV PKA. The ion insertion rate,  $\dot{G}$ , is calculated from the parameters in Table 1 as:

$$\dot{G} = \frac{\dot{\gamma} \rho_a \Omega}{N_{\text{NRT}}} \quad (4)$$

---

<sup>3</sup>Note that what is referred to as ‘1D diffusion’ in the context of irradiation damage is the migration along rectilinear paths of defects evolving in a 3D setting.

where  $\dot{\gamma}$  is the dpa rate,  $\rho_a$  the atomic density of W, and  $\Omega$  the simulation volume referred to in A. For sufficient statistics, it is desirable to accelerate the ion insertion rate as much as possible, which implies using as large a value of  $\Omega$  as reasonably possible. In this work we use  $\Omega = 10^{-12} \text{ cm}^{-3}$ .

## 3 Results

### 3.1 Cluster size distributions

Figure 4 shows the computed SIA and vacancy cluster size distributions at the end of the irradiation period and after a room temperature annealing of one hour of duration. In both cases, the experimentally measured defect size distributions (corresponding to the ‘after annealing’ simulation results) are shown for comparison.

Figure 4(a) displays the SIA cluster size distribution in the ‘as irradiated’ and ‘after annealed’ conditions. The scatter in the model defect size distributions is due to the stochastic nature of our simulations, which, for a given parameter set, yield different but statistically valid results when repeated several times. Furthermore, the statistical variance increases with cluster size due to limited statistics. As the figure shows, the difference between the as-irradiated and annealed size distributions is most visible for cluster sizes with  $n < 30$ . This is a direct consequence of the high mobility of  $I_1$  and  $I_2$  defects, whose populations, in the absence of irradiation, are partitioned in the following manner:

- (i) A portion is consumed via recombination with vacancies and vacancy clusters.
- (ii) Another fraction is absorbed by existing SIA loops, which contributes to their steady –albeit modest– growth during the annealing.
- (iii) Emission of single SIA from small SIA clusters, enabled by modest binding energies of clusters with  $n < 10$  (see Table 3).

Our results show that the defect size distributions match the experimental distribution for large cluster sizes. Interestingly, the agreement is remarkably accurate if one considers the lower edge (convex hull) of the simulated statistical distributions. For smaller defects, the agreement improves after the simulated annealing, owing principally to a decline in the populations of small SIA clusters through dissociation and recombination.

Figure 4(b) shows the vacancy cluster size distribution functions for the as-irradiated and annealed conditions. The figure shows the extent of TEM size resolution regions assuming planar loops ( $n > 30$ ) (as a reference, for globular clusters,  $n > 110$ ). Qualitatively, the vacancy cluster population displays a size distribution similar to its self-interstitial counterpart, with large scatters in the cluster populations for large defect sizes. However, in this case, unlike for SIA defects, the plot shows a stable monovacancy contribution in the as-irradiated condition that reaches very high concentrations. This is a consequence of the negligible mobility of vacancies at 290 K, which leads to a high retention of monovacancies in the material. After the annealing, most of the di-vacancy ( $V_2$ ) population disappears on account of its thermal instability (negative binding energy, see Table 3), and a concentration maximum develops for the  $V_4$  cluster. For its part, the experimental size distribution underestimates the concentrations of vacancy clusters with  $n < 20$ , both in the as-irradiated and annealed conditions, but displays excellent agreement with the simulation results at larger cluster sizes.

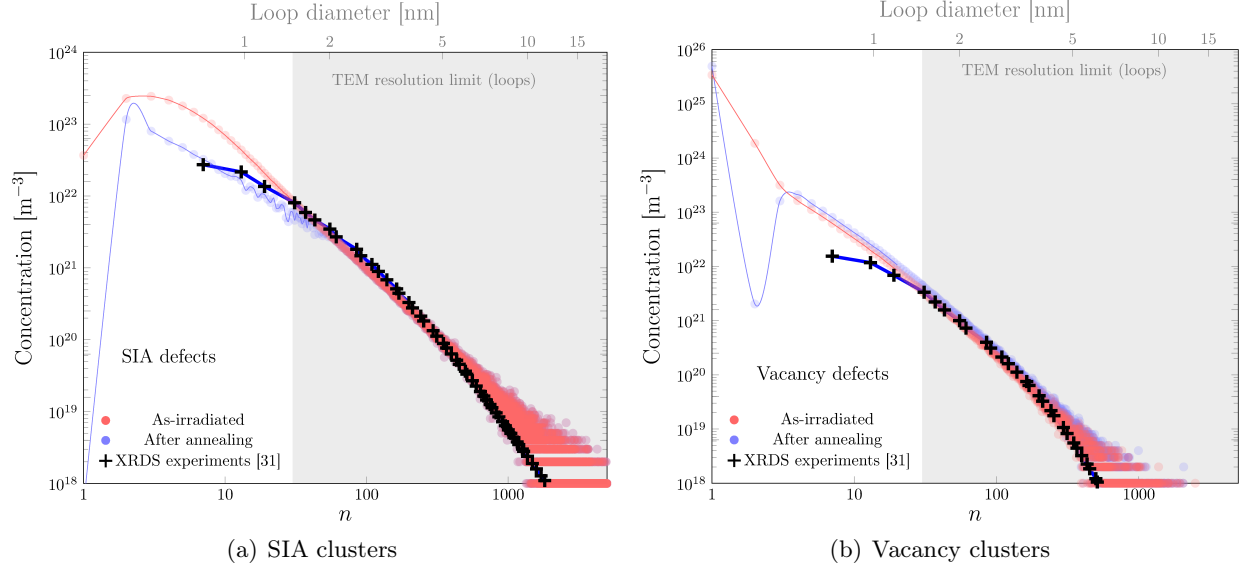


Figure 4: Simulated cluster size distributions at end of irradiation (0.008 dpa) and after annealing for 24 hours at room temperature. (a) SIA clusters. (b) Vacancy clusters. The shaded region represents the range of visible clusters by conventional TEM. For loops, this limit ( $n = 30$ ) is obtained by setting the diameter of a circular disc to a minimum diameter of 1.5 nm.

### 3.2 Defect cluster evolution

Figure 5 shows the evolution of the SIA and vacancy subpopulations as a function of irradiation time. Each population is partitioned into single point defects ( $I_1$  and  $V_1$ ), all clusters ( $I_n$ ,  $n > 2$ ), and loops and voids above the TEM resolution limit ( $n > 30$  and  $n > 110$ , respectively). The evolution of SIA defects is displayed in Fig. 5(a), where the unstable nature of the single SIA population is clear from its relatively low concentrations and highly volatile time evolution. This is, as discussed above, a direct consequence of their high mobility and transient behavior. In contrast, the SIA cluster populations exhibit well-defined, monotonically-increasing trends throughout the entire irradiation process.

The evolution of the vacancy clusters is shown in Fig. 5(b). In this case, the monovacancy population is seen to be stable and grow at the same rate as larger clusters, although in much larger concentrations. Indeed, more than 90 Clusters of both types are seen to increase linearly, indicating that the system is found in a transient stage of defect accumulation and has not reached saturation yet.

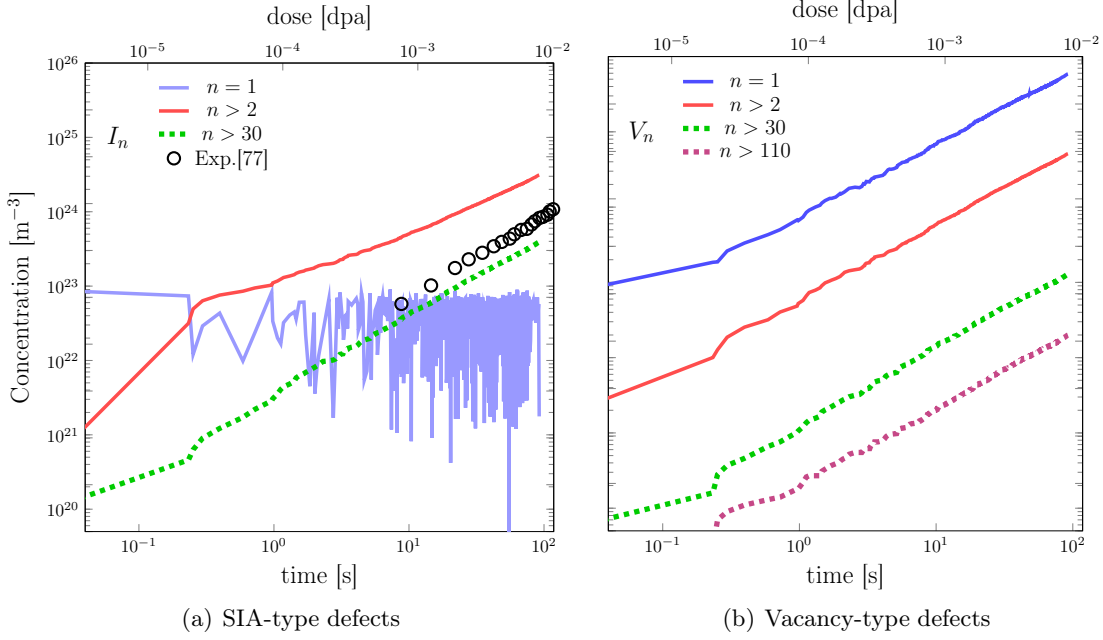


Figure 5: Evolution with time of the concentrations of (a) SIA ( $I_n$ ) and (b) vacancy ( $V_n$ ) clusters. Each plot tracks the evolution of single SIA and monovacancies (blue curves), clusters with more than two defects (red), and clusters beyond the TEM resolution limit (dashed green) for loops with lenticular shape ( $n > 30$ ) and voids with spherical shape ( $n > 110$ ). The TEM visible SIA cluster concentrations measured by Reza et al. using 20-MeV W ions at room temperature are shown in pane (a) for comparison [77].

## 4 Discussion

### 4.1 Capabilities of physics-based numerical simulation model

We have identified four essential factors without which model predictions would not have achieved the high degree of agreement with the experimental data. In no particular order, these factors are: (i) accurately capturing the amount of defects produced in cascades as a function of PKA energy; (ii) one-dimensional, athermal SIA diffusion; (iii) universal scaling law of cluster sizes for defects generated in displacement cascades (independent of PKA energy); and (iv) consideration of the disproportionate importance of the high-energy tail of the PKA energy distribution function. All four have been implemented in our models, jointly contributing to the accuracy of the simulations and the agreement with experiments. Point (i) ensures that a sufficient number of defects are inserted to account for the large clusters observed experimentally. Point (ii) maintains a high SI mobility at low temperatures, which controls recombination with vacancies and post-cascade SIA loop growth. Point (iii) guarantees that the defect clusters inserted into the simulation volume appear with the correct sizes from the beginning. Finally, point (iv) plays the crucial role of ensuring that the material is seeded with few but important large immobile dislocation loops, which act as a stable substrate on which further irradiation damage accumulates and evolves.

The four factors above pertain to the physics of irradiation damage in W, and are in principle agnostic to the model through which they are implemented. These may include okMC [14, 4, 29], MFRT [78, 24, 79], or our hybrid method SCD, which builds on advantageous features of both: (i) a mean-field description of the defect populations for computational efficiency and reaching high

irradiation doses, and (ii) uses a kinetic Monte Carlo solver to avoid numerical solution bottlenecks in MFRT and provide a meaningful statistical variance to assess numerical errors.

Key to the model validity is the realization that most of the energetics employed are obtained with atomistic simulations. Both semi-empirical potential and DFT-based atomistic calculations have reached an impressive degree of accuracy, which carries over to the models and decisively contributes to their validity.

## 4.2 Discussion on literature on heavy ion irradiation of W

The majority of heavy-ion irradiation studies in W have been performed at temperatures near the operational window for fusion applications,  $>500^{\circ}\text{C}$ . Under such conditions, monovacancies are mobile, leading to the formation of vacancy clusters and voids of various sizes depending on irradiation conditions. Irradiations with 18-MeV self-ions at 500 and  $800^{\circ}\text{C}$  up to 0.2 dpa by Hwang et al. [80] revealed both dislocation loops and voids, with average sizes of, respectively, 3.1 and  $1.0\sim1.5$  nm. These vacancy clusters are at or below the visibility threshold in TEM, which hampers our ability to extract statistically meaningful counts of these defects. This limitation can be addressed using positron annihilation spectroscopy (PAS) (e.g., refs. [81, 32]), which can detect down to monovacancies. Early PAS tests have determined with precision the temperature for Stage III recovery, which was found to be between 523 and 573 K [81]. More recent PAS results of irradiations with 18-MeV self-ions to 0.0085 dpa indicate that approximately 98

In terms of room temperature tests, Wang et al. [82] irradiated W foils with 6.0-MeV Cu ions up to a damage level of 0.6 dpa, finding a microstructure dominated by dislocation loops with an average size of 8.0 nm ( $n \approx 870$ ) at concentrations greater than  $10^{22} \text{ m}^{-3}$ . These are one to two orders of magnitude larger than what we report here, consistent with a total irradiation dose 75 times higher than ours. These authors also pointed out that the loop microstructure saturates after 0.2 dpa of irradiation, which is not seen here to our lower doses, as demonstrated by the increasing trends in Fig. 5. In contrast, their finding that the main vacancy defects were monovacancies and small clusters is consistent with our calculations. A separate work involving 20-MeV self-ion irradiation of polycrystal W with an average grain size of 40 microns [77] reports the accumulation of visible defect clusters in the amounts shown in Fig. 5(a). In the range of doses common to our study and that in ref. [77], and despite the differences in the material microstructure and the irradiation conditions, there is very good quantitative agreement between our simulations (for TEM-visible defects) and the experimental data. In particular, our simulations provide an almost exact match of the time evolution of the cluster population observed experimentally.

Finally, being a mean-field approach, our study does not discriminate between different Burgers vectors for the dislocation loops. Recent experiments using of 800-keV Kr ions at  $400^{\circ}\text{C}$  suggest a 50/50 partition between  $1/2\langle 111 \rangle$  and  $\langle 100 \rangle$  Burgers vectors [49]. Likewise, TEM specimens irradiated with 1.2-MeV W ions up to 0.017 dpa at room temperature indicate a similar loop coexistence [83]. While these results may be at odds with some atomistic simulations, which predict a clear general preponderance of  $1/2\langle 111 \rangle$  loops [54, 84, 85], better agreement is found if only vacancy-type loops are considered.

## 4.3 Comparison between model predictions and experimental data

The simulated defect cluster distributions show excellent overall agreement with the experimental measurements across nearly four orders of magnitude in concentration. The XRDS measurements provide sufficient resolution for clusters with  $n > 8$ . As such, there are no experimental data against which to compare the model predictions directly in the  $1 < n < 8$  range. For SIA defects (Fig.

4(a)) in the as-irradiated condition, the populations of clusters with  $n < 30$  show an increasing discrepancy between the measured data as the cluster size decreases. This discrepancy is mitigated in the annealed condition, suggesting that the combined effect of thermal coarsening and monomer dissociation during a prolonged annealing period is important at low cluster sizes. Additionally, part of the deviation can be attributed to the use of closed-form size-dependent cross-sections for dislocation loops in the interpretation of XRDS signals [31], which are known to misrepresent the structure of SIA clusters with  $n < 10$  [86].

For the vacancy cluster subpopulation, Fig. 4(b), the disparity between the calculations and measurements is more pronounced at small sizes than for SIA defects, even in the annealed condition. In addition to the signal resolution factor discussed for SIA clusters, the XRDS cross sections used for small vacancy clusters are also obtained assuming ‘loop’-like defect structures. However, as discussed in the previous subsection, PAS experiments have conclusively established the globular nature of vacancy clusters with  $n < 10$ . Indeed, recent measurements by Hu et al. [32] obtained from experiments conducted at 500°C with 20-MeV ions up to 0.02 dpa demonstrate high concentrations of  $V_n$  clusters with  $n < 10$ .

What we can say with certainty is that, for both SIA and vacancy clusters with  $n > 30$ , the agreement between the model predictions and the experimental data is outstanding, which adds a high level of confidence to the underlying physical principles behind the simulation models. Future work will include scenarios corresponding to different irradiation conditions, particularly temperature, particle energy, and particle mass (to control the PKA energy spectrum), with the ultimate goal of projecting to fusion energy conditions in leading conceptual designs.

## 5 Conclusions

We finish the paper with our most important conclusions and summary points.

- We have assembled a number of fundamental physics features that have recently emerged in the literature into a numerical model for irradiation damage accumulation in tungsten. The model includes athermal SIA diffusion along rectilinear paths, atomistically-generated Frenkel-pair insertion correlations and cluster size distributions, and large sampling volumes to ensure that an adequate sampling of the high-energy tail of the PKA energy distribution is effectuated.
- The model relies heavily on pre-computed atomistic properties and contains no adjustable parameters.
- The model has been validated mainly through a series of XRDS experiments of self-ion-irradiated single-crystal W at room temperature. The experiments were designed as to facilitate comparison with the model by simplifying the irradiation conditions and eliminating microstructural complexities.
- The model is also in very good agreement with other independent works on W irradiated at room temperature.
- Model predictions are in excellent agreement with XRDS measurements of vacancy and SIA cluster size distributions at the end of a 0.085-dpa irradiation stage followed by a long annealing at room temperature. This agreement holds over a large range of cluster sizes for both self-interstitial and vacancy defect types.

- Finally, the model provides quantitative predictions in the missing cluster size range outside the resolution limit of XRDS, thus complementing experimental data beyond what experiments can access.

## Acknowledgments

The authors acknowledge financial support from the U.S. Department of Energy, Office of Fusion Energy Sciences (DOE-FES) under contracts DE-SC0018410 (S.H. and J.M.) and DE-SC0022528 (B.S. and G.T.). This work used computational and storage services associated with the Hoffman2 Cluster which is operated by the UCLA Office of Advanced Research Computing's Research Technology Group. The authors acknowledge the use of facilities and instrumentation at the UC Irvine Materials Research Institute (IMRI) which is supported in part by the National Science Foundation through the UC Irvine Materials Research Science and Engineering Center (grant No. DMR-2011967).

## A Brief review of the stochastic cluster dynamics method

The accumulation of defects during irradiation is simulated using the stochastic cluster dynamics (SCD) model. SCD is a stochastic variant of the mean-field rate theory technique which relies on stochastic sampling of the underlying master equation for defect cluster evolution [87, 88]. Instead of deterministically solving exceedingly large sets of partial differential equations (PDE) of the concentrations of defects, as in standard MFRT, SCD evolves an integer-valued defect population  $N_i$  in a finite material volume  $\Omega$ , thus avoiding exponential growth in the number of ODEs. This makes SCD ideal to treat problems where the dimensionality of the cluster size space is high, e.g., when multispecies simulations are of interest [89, 22, 90].

SCD recasts the standard ODE system into stochastic equations of the form:

$$\frac{dN_i}{dt} = \tilde{g}_i + \tilde{s}_l N_l - \left[ \tilde{s}_i N_i + \sum_{\alpha} \tilde{s}_{\alpha i} N_i \right] + \sum_j \left[ \sum_k \tilde{K}_{jk} N_j N_k - \tilde{K}_{ij} N_j N_i \right] \quad (5)$$

where the set  $\{\tilde{g}, \tilde{s}, \tilde{K}\}$  represents the reaction rates for defect insertion, thermal dissociation, and annihilation at sinks, and binary reactions occurring inside  $\Omega$ . Subindices  $j$  and  $k$  refer to all distinct defect species present in the system, whereas the subindex  $\alpha$  refers to the type of sinks available to absorb defects ('d' for dislocations, 'gb' for grain boundaries, 'ppt' for precipitates). The subindices in the expression satisfy  $l - 1 = i$  and  $j + k = i$  (reflecting dissociation by monomer emission and association of complementary clusters, respectively). Equation (5) can be straightforwardly extended to partial differential equations to capture diffusion due to defect concentration gradients [91].

Equation (5) is solved using the residence-time algorithm by sampling, selecting, and executing events from the set of rates  $\{\tilde{g}, \tilde{s}, \tilde{K}\}$  [87]. The volume  $\Omega$  is arbitrary, although its minimum value is subjected to the numerical stability criterion:

$$\Omega^{\frac{1}{3}} > \ell \quad (6)$$

with

$$\ell = \max_i \{l_i\} \quad (7)$$

$$l_i = \sqrt{D_i \tau_i} \quad (8)$$

where  $D_i$  and  $\tau_i$  are the diffusivity and the lifetime of mobile species  $i$ ,  $\tau_i^{-1} = \tilde{s} + \sum_j \tilde{K}_{ij} N_j$ . For consistency with the experimental conditions provided above, here we consider vacancies, self-interstitial atoms, and any cluster combination thereof.

As a practical note, under certain conditions the volume  $\Omega$  can be rescaled for improved computational efficiency, leading to an accelerated defect cluster evolution. A quantitative demonstration of volume rescaling applied to a selected group of defect clusters is provided in ref. [92]. For more information about the model, the reader is referred to past publications from the authors [87, 88, 91].

## A.1 Defect insertion rates

The defect insertion rates,  $\tilde{g}_i$  in eq. (5), are obtained for each defect type by multiplying the volumetric insertion rates ( $g_i$  in Fig. 1) times the simulation volume  $\Omega$ . In turn, the  $g_i$  rates are set by the ion insertion rate, defined in eq. (4), followed by sampling  $C(E)$  recursively until the total ion energy expended on lattice damage, i.e., 2.65 MeV, is reached (see Sec. 2.2 for more details)<sup>4</sup>. During each sampling, defect distributions obeying eqs. (2) and using the scaling laws extracted from Fig. 3 are generated, and an array of species  $i$  is created. These species are then added to the simulation volume and let to evolve according to eqs. (5).

In order to appropriately sample the entire range of cluster sizes, set by the histograms in Fig. 3, it is desirable to produce PKA with energies greater than 50 keV. Without them, the large clusters observed experimentally with  $n > 50$  would not be created in the simulations. However, due to the low probability of producing PKA with those energies (it is worth keeping in mind that the average PKA energy in the present irradiations is <1 keV), large numbers of PKA samplings must be instantiated. This can only be achieved by maintaining sufficiently high values of  $\dot{G}$  (eq. (4)), which is directly proportional to the simulation volume  $\Omega$ . Thus, a crucial part of our model is ensuring that  $\Omega$  is kept above a minimum limit that guarantees adequate sampling of  $C(E)$  and the cluster size power laws.

## A.2 Defect energetics

Defect mobilities display an Arrhenius temperature dependence,  $D(T) = D_0 \exp(-E_m/kT)$ , where  $D_0$  is the diffusion prefactor and  $E_m$  is the migration energy. As indicated in Sec. 2.3.3, here we consider mobilities of single and di-interstitials, as well as monovacancies, with their diffusion parameters given in Table 2.

We also consider thermal dissociation of SIA and vacancy clusters by emission of monomers. As indicated in Fig. 1, the dissociation rate scales with the factor  $\exp(-E_n^b/kT)$ , where  $E_n^b$  is the binding energy of a monomer (monovacancy or single SIA) to a cluster of size  $n$ . Atomistic calculations of SIA and vacancy clusters up to  $n = 8$  exist in the literature [18, 14, 84]. Specifically, here we use the DFT data by Becquart et al. [95], as listed in Table 3. For larger sizes, the binding energies are obtained as:

$$E_n^b = (E^f(1) + E^f(n-1)) - E^f(n) = E^f(1) - (E^f(n) - E^f(n-1)) \approx E^f(1) - \frac{dE^f(n)}{dn} \quad (9)$$

where  $E^f(n)$  is the formation energy of a cluster of size  $n$ . Here we assume that vacancy clusters adopt a globular shape for  $8 \leq n < 30$ , whose formation energies are well captured using the

---

<sup>4</sup>Note that using the ASTM-recommended value for the threshold displacement energy of W of  $E_{th}=90$  eV, this amount of energy would result in the creation of  $N_{NRT} = \eta E/2E_{th} \approx 2.35 \times 10^7$  Frenkel pairs according to the NRT formalism [93] when an efficiency of  $\eta = 0.8$  is used. However, this is known to grossly overpredict the number of defects actually created during irradiation [94].

capillary approximation, i.e.,  $E^f(n) \sim n^{2/3}$  [14, 91]. The expression for the binding energies in this size range is given in Table 3. Finally, we assume that vacancy clusters with  $n \geq 30$  and SIA clusters with  $n \geq 8$  appear as prismatic loops with energies given by the expression [84, 85]:

$$E_f(n) = a_0 \sqrt{n} \log n + a_1 \sqrt{n} + a_2 \quad (10)$$

from which, after operating with eq. (9), we obtain the final expression for the binding energy of loops:

$$E_n^b = E^f(1) - \frac{a_0}{2\sqrt{n}} \log n + \frac{2a_0 + a_1}{2\sqrt{n}} = E^f(1) - \frac{a_0}{2\sqrt{n}} \left( \log n - 2 - \frac{a_1}{a_0} \right) \quad (11)$$

$a_0$  and  $a_1$  are numerical coefficients given for each type of loop in Table 3.

Table 3: Binding energies of monomers to  $I_n$  and  $V_n$  clusters used in the simulations. All data from reference [14]. Values for  $E^f(I_1)$  and  $E^f(V_1)$  are 9.96 and 3.23 eV, respectively [17].

Species	$E_n^b$ [eV]
$I_2$	2.12
$I_3$	3.02
$I_4$	3.60
$I_5$	3.98
$I_6$	4.27
$I_7$	5.39
$n > 7$	$E^f(1) - \frac{a_0}{2\sqrt{n}} \log n + \frac{2a_0 + a_1}{2\sqrt{n}}$ $a_0 = 3.394 \quad a_1 = 7.081$
$V_2$	-0.10
$V_3$	0.04
$V_4$	0.64
$V_5$	0.72
$V_6$	0.89
$V_7$	0.72
$7 < n \leq 30$	$E^f(V_1) + 1.71 (E^b(V_2) - E^f(V_1)) [n^{2/3} - (n-1)^{2/3}]$
$n > 30$	$E^f(1) - \frac{a_0}{2\sqrt{n}} \log n + \frac{2a_0 + a_1}{2\sqrt{n}}$ $a_0 = 4.155 \quad a_1 = -0.01$

## References

- [1] W. Weber, Models and mechanisms of irradiation-induced amorphization in ceramics, *Nuclear Instruments and Methods in Physics Research Section B: Beam Interactions with Materials and Atoms* 166 (2000) 98–106.
- [2] C. H. Woo, Modeling irradiation damage accumulation in crystals, in: *Handbook of Materials Modeling: Methods*, Springer, 2005, pp. 959–986.
- [3] B. D. Wirth, How does radiation damage materials?, *Science* 318 (5852) (2007) 923–924.
- [4] C. Becquart, C. Domain, Modeling microstructure and irradiation effects, *Metallurgical and Materials Transactions A* 42 (4) (2011) 852–870.
- [5] S. Dudarev, Density functional theory models for radiation damage, *Annual Review of Materials Research* 43 (1) (2013) 35–61.
- [6] X. Xiao, D. Terentyev, H. Chu, H. Duan, Theoretical models for irradiation hardening and embrittlement in nuclear structural materials: a review and perspective, *Acta Mechanica Sinica* 36 (2) (2020) 397–411.
- [7] Y. Fan, Atomistic modeling of microstructural defect evolution in alloys under irradiation: A comprehensive review, *Applied Sciences* 15 (16) (2025) 9110.
- [8] M. Rieth, S. L. Dudarev, S. G. De Vicente, J. Aktaa, T. Ahlgren, S. Antusch, D. Armstrong, M. Balden, N. Baluc, M.-F. Barthe, et al., Recent progress in research on tungsten materials for nuclear fusion applications in europe, *Journal of Nuclear Materials* 432 (1-3) (2013) 482–500.
- [9] M. Rieth, S. Antusch, C. Bonnekoh, A. Hoffmann, W. Knabl, P. Lied, Tungsten alloys r&d program at kit, in: *Fusion Energy Technology R&D Priorities*, Elsevier, 2025, pp. 53–60.
- [10] J. Marian, C. Becquart, C. Domain, S. Dudarev, M. Gilbert, R. Kurtz, D. Mason, K. Nordlund, A. Sand, L. Snead, et al., Recent advances in computational materials modeling of tungsten as plasma-facing material for fusion energy applications, *Nucl. Fusion* 57 (9).
- [11] J. Yu, M. Simmonds, M. Baldwin, R. Doerner, Deuterium retention in re-solidified tungsten and beryllium, *Nuclear Materials and Energy* 18 (2019) 297 – 306.  
doi:<https://doi.org/10.1016/j.nme.2019.01.011>.  
URL <http://www.sciencedirect.com/science/article/pii/S2352179118302436>
- [12] Y. Qian, M. R. Gilbert, L. Dezerald, D. Cereceda, Using first-principles calculations to predict the mechanical properties of transmuting tungsten under first wall fusion power-plant conditions, *Journal of Physics: Condensed Matter* 33 (34) (2021) 345901.
- [13] C. McElfresh, A. Ghazari, N. Ghoniem, J. Marian, Fracture modes and grain growth of tungsten during extreme cyclic heating, *Journal of Nuclear Materials* 599 (2024) 155196.
- [14] C. S. Becquart, C. Domain, U. Sarkar, A. Debacker, M. Hou, Microstructural evolution of irradiated tungsten: Ab initio parameterisation of an okmc model, *Journal of nuclear materials* 403 (1-3) (2010) 75–88.
- [15] L. Chen, Y. Liu, H. Zhou, S. Jin, Y. Zhang, G. Lu, Stability and diffusion properties of self-interstitial atoms in tungsten: a first-principles investigation, *Science China Physics, Mechanics and Astronomy* 55 (4) (2012) 614–618.

[16] J. Boisse, C. Domain, C. Becquart, Modelling self trapping and trap mutation in tungsten using dft and molecular dynamics with an empirical potential based on dft, *Journal of Nuclear Materials* 455 (1-3) (2014) 10–15.

[17] L. Ventelon, F. Willaime, C.-C. Fu, M. Heran, I. Ginoux, Ab initio investigation of radiation defects in tungsten: Structure of self-interstitials and specificity of di-vacancies compared to other bcc transition metals, *Journal of Nuclear Materials* 425 (1-3) (2012) 16–21.

[18] J. Fikar, R. Schäublin, Molecular dynamics simulation of radiation damage in bcc tungsten, *Journal of nuclear materials* 386 (2009) 97–101.

[19] G. Nandipati, W. Setyawan, H. L. Heinisch, K. J. Roche, R. J. Kurtz, B. D. Wirth, Displacement cascades and defect annealing in tungsten, part ii: Object kinetic monte carlo simulation of tungsten cascade aging, *Journal of Nuclear Materials* 462 (2015) 338–344.

[20] J. Liu, J. Byggmästar, Z. Fan, P. Qian, Y. Su, Large-scale machine-learning molecular dynamics simulation of primary radiation damage in tungsten, *Physical Review B* 108 (5) (2023) 054312.

[21] J. Liu, J. Byggmästar, Z. Fan, B. Bai, P. Qian, Y. Su, Utilizing a machine-learned potential to explore enhanced radiation tolerance in the monbtavw high-entropy alloy, *Journal of Nuclear Materials* (2025) 156004.

[22] J. Marian, T. L. Hoang, Modeling fast neutron irradiation damage accumulation in tungsten, *Journal of Nuclear Materials* 429 (1) (2012) 293 – 297. doi:<https://doi.org/10.1016/j.jnucmat.2012.06.019>. URL <http://www.sciencedirect.com/science/article/pii/S0022231151200308X>

[23] N. Castin, A. Bakaev, G. Bonny, A. E. Sand, L. Malerba, D. Terentyev, On the onset of void swelling in pure tungsten under neutron irradiation: An object kinetic monte carlo approach, *Journal of Nuclear Materials* 493 (2017) 280–293.

[24] M. Jin, C. Permann, M. P. Short, Breaking the power law: Multiscale simulations of self-ion irradiated tungsten, *Journal of Nuclear Materials* 504 (2018) 33–40.

[25] N. Castin, G. Bonny, A. Bakaev, C. Ortiz, A. Sand, D. Terentyev, Object kinetic monte carlo model for neutron and ion irradiation in tungsten: Impact of transmutation and carbon impurities, *Journal of nuclear materials* 500 (2018) 15–25.

[26] D. R. Mason, A. E. Sand, S. L. Dudarev, Atomistic-object kinetic monte carlo simulations of irradiation damage in tungsten, *Modelling and simulation in materials science and engineering* 27 (5) (2019) 055003.

[27] P.-W. Hou, Y.-H. Li, Z.-Z. Li, L.-F. Wang, X. Gao, H.-B. Zhou, H. Song, G.-H. Lu, Influence of helium on the evolution of irradiation-induced defects in tungsten: an object kinetic monte carlo simulation, *Chinese Physics B* 30 (8) (2021) 086108.

[28] H.-Z. Ma, Y.-H. Li, Y.-Z. Niu, D. Terentyev, Z. Yang, H.-B. Zhou, G.-H. Lu, Initial microstructure and temperature dependence of irradiation defects evolution in tungsten, *Journal of Nuclear Materials* 591 (2024) 154932.

[29] J. Wu, J.-P. Balbuena, V. Jantunen, M. J. Caturla, F. Granberg, Influence of initial damage distribution and sinks in fusion materials: A parametric okmc study of w vs fe, *Nuclear Materials and Energy* (2025) 101975.

[30] S. Mohamed, Q. Yuan, D. Litvinov, J. Gao, E. Gaganidze, D. Terentyev, H.-C. Schneider, J. Aktaa, Investigation of microstructural evolution of irradiation-induced defects in tungsten: an experimental–numerical approach, *Nuclear Fusion* 65 (6) (2025) 066007.

[31] B. Schwendeman, B. C. Larson, M. J. Simmonds, T. Schwarz-Selinger, S. Faulhaber, M. J. Baldwin, G. R. Tynan, Integral x-ray diffuse scattering for studying irradiation-induced dislocation loops in single crystals, *Journal of Applied Crystallography* 58 (2) (2025) 302–320.

[32] Z. Hu, J. Wu, Q. Yang, F. Jomard, F. Granberg, M.-F. Barthe, New insight into the quantifying vacancy distribution in self-ion-irradiated tungsten: A combined experimental and computational study, *Nano Letters*.

[33] J. Zavašnik, A. Šestan, T. Schwarz-Selinger, K. Hunger, E. Lu, F. Tuomisto, K. Nordlund, E. Punzón-Quijorna, M. Kelemen, J. Predrag, et al., Microstructural analysis of tungsten single crystals irradiated by mev w ions: The effect of irradiation dose and temperature, *Materials Characterization* 224 (2025) 115050.

[34] W. Wolfer, M. Ashkin, Stress- induced diffusion of point defects to spherical sinks, *Journal of Applied Physics* 46 (2) (1975) 547–557.

[35] L. Malerba, C. S. Becquart, C. Domain, Object kinetic monte carlo study of sink strengths, *Journal of Nuclear Materials* 360 (2) (2007) 159–169.

[36] S. Golubov, R. Stoller, S. Zinkle, A. Ovcharenko, Kinetics of coarsening of helium bubbles during implantation and post-implantation annealing, *Journal of Nuclear Materials* 361 (2-3) (2007) 149–159.

[37] N. M. Ghoniem, Rate theory of radiation damage, *Handbook of Materials Modeling: Applications: Current and Emerging Materials* (2020) 2215–2242.

[38] G. Odette, On mechanisms controlling swelling in ferritic and martensitic alloys, *Journal of Nuclear Materials* 155 (1988) 921–927.

[39] Y. G. Korobeinikov, Calculation of three-body recombination rate constants, *Combustion, Explosion and Shock Waves* 11 (6) (1975) 737–743.

[40] K. Xu, B. G. Thomas, Y. Wu, H. Wang, H. Kong, Z. Wu, Grouping methods of cluster dynamics model for precipitation kinetics, *Metals* 10 (12) (2020) 1685.

[41] Y. Cao, D. T. Gillespie, L. R. Petzold, Efficient step size selection for the tau-leaping simulation method, *The Journal of chemical physics* 124 (4).

[42] J. Marian, V. V. Bulatov, Stochastic cluster dynamics method for simulations of multispecies irradiation damage accumulation, *Journal of Nuclear Materials* 415 (1) (2011) 84–95.

[43] M. Anand, B. Pande, R. Agarwala, Recovery in neutron irradiated tungsten, *Radiation Effects* 39 (3-4) (1978) 149–155.

[44] P. Nambissan, P. Sen, Positron annihilation study of the annealing behaviour of alpha induced defects in tungsten, *Radiation Effects and Defects in Solids* 124 (2) (1992) 215–221.

[45] J. DiCarlo, C. Snead Jr, A. Goland, Stage-i interstitials in electron-irradiated tungsten, *Physical Review* 178 (3) (1969) 1059.

[46] L. Keys, J. Moteff, Neutron irradiation and defect recovery of tungsten, *Journal of Nuclear Materials* 34 (3) (1970) 260–280. doi:[https://doi.org/10.1016/0022-3115\(70\)90193-5](https://doi.org/10.1016/0022-3115(70)90193-5). URL <https://www.sciencedirect.com/science/article/pii/0022311570901935>

[47] D. N. Seidman, On the point-defect annealing mechanism for stage iii recovery in irradiated or quenched tungsten, *Scripta Metallurgica* 13 (4) (1979) 251–257.

[48] K. Wilson, M. Baskes, D. Seidman, An in situ field-ion microscope study of the recovery behavior of ion-irradiated tungsten and tungsten alloys, *Acta metallurgica* 28 (1) (1980) 89–102.

[49] R.-Y. Zheng, W.-Z. Han, Comparative study of radiation defects in ion irradiated bulk and thin-foil tungsten, *Acta Materialia* 186 (2020) 162–171. doi:<https://doi.org/10.1016/j.actamat.2019.12.053>. URL <https://www.sciencedirect.com/science/article/pii/S1359645420300094>

[50] L. N. Clowers, Z. Jiao, G. S. Was, Synergies between h, he and radiation damage in dual and triple ion irradiation of candidate fusion blanket materials, *Journal of Nuclear Materials* 565 (2022) 153722.

[51] J. F. Ziegler, J. P. Biersack, U. Littmark, *The Stopping and Range of Ions in Matter*, Pergamon Press, New York, 1985. doi:<http://www.srim.org>. URL <http://www.srim.org>

[52] W. Setyawan, G. Nandipati, K. J. Roche, H. L. Heinisch, B. D. Wirth, R. J. Kurtz, Displacement cascades and defects annealing in tungsten, part i: Defect database from molecular dynamics simulations, *Journal of Nuclear Materials* 462 (2015) 329–337.

[53] J. Marian, W. Setyawan, Y. Yang, A. Manzoor, W. Zhong, J. R. Trelewicz, J. Yu, E. Peterson, Y. Katoh, L. Snead, et al., Computational materials assessment of the d/li-stripping neutron source as a prototypical facility for fusion materials testing, *Current Opinion in Solid State and Materials Science* 38 (2025) 101231.

[54] J. Byggmästar, V.-M. Yli-Suutala, A. Fellman, J. Åström, J. Westerholm, F. Granberg, Four regimes of primary radiation damage in tungsten, *arXiv preprint arXiv:2503.02710*.

[55] T. Troev, N. Nankov, T. Yoshiie, Simulation of displacement cascades in tungsten irradiated by fusion neutrons, *Nuclear Instruments and Methods in Physics Research Section B: Beam Interactions with Materials and Atoms* 269 (6) (2011) 566–571.

[56] A. E. Sand, S. Dudarev, K. Nordlund, High-energy collision cascades in tungsten: Dislocation loops structure and clustering scaling laws, *Europhysics Letters* 103 (4) (2013) 46003.

[57] B. Wirth, G. Odette, D. Maroudas, G. Lucas, Dislocation loop structure, energy and mobility of self-interstitial atom clusters in bcc iron, *Journal of nuclear materials* 276 (1-3) (2000) 33–40.

[58] J. Marian, B. D. Wirth, R. Schäublin, G. Odette, J. M. Perlado, Md modeling of defects in fe and their interactions, *Journal of nuclear materials* 323 (2-3) (2003) 181–191.

[59] T. Faney, B. Wirth, Spatially dependent cluster dynamics modeling of microstructure evolution in low energy helium irradiated tungsten, *Modelling and Simulation in Materials Science and Engineering* 22 (6) (2014) 065010.

[60] F. Dausinger, H. Schultz, Long-range migration of self-interstitial atoms in tungsten, *Physical Review Letters* 35 (26) (1975) 1773.

[61] K. Arakawa, M.-C. Marinica, S. Fitzgerald, L. Proville, D. Nguyen-Manh, S. L. Dudarev, P.-W. Ma, T. D. Swinburne, A. M. Goryaeva, T. Yamada, et al., Quantum de-trapping and transport of heavy defects in tungsten, *Nature Materials* 19 (5) (2020) 508–511.

[62] W. H. Zhou, C. G. Zhang, Y. G. Li, Z. Zeng, Creeping motion of self interstitial atom clusters in tungsten, *Scientific reports* 4 (1) (2014) 5096.

[63] W. Zhou, Y. Li, L. Huang, Z. Zeng, X. Ju, Dynamical behaviors of self-interstitial atoms in tungsten, *Journal of nuclear materials* 437 (1-3) (2013) 438–444.

[64] S. long Wen, H. Zhang, K. H. He, X. S. Yang, H. N. Cui, M. Pan, Z. Huang, Y. Zhao, The study of defect structure in tungsten: Rotation and migration property for the self-interstitial atoms, *Fusion Engineering and Design* 124 (2017) 1122–1126.

[65] J. Wang, Q. Hou, B. Zhang, Migration behavior of self-interstitial defects in tungsten and iron, *Solid State Communications* 325 (2021) 114158.

[66] T. Amino, K. Arakawa, H. Mori, Detection of one-dimensional migration of single self-interstitial atoms in tungsten using high-voltage electron microscopy, *Scientific reports* 6 (1) (2016) 26099.

[67] P. M. Derlet, D. Nguyen-Manh, S. Dudarev, Multiscale modeling of crowdion and vacancy defects in body-centered-cubic transition metals, *Physical Review B—Condensed Matter and Materials Physics* 76 (5) (2007) 054107.

[68] X. Zhou, A. Barnett, E. H. Mang, M. L. Falk, M. L. Taheri, J. Marian, Self-interstitial atom properties in nb–mo–ta–w alloys, *Computational Materials Science* 234 (2024) 112765.

[69] T. Amino, K. Arakawa, H. Mori, Activation energy for long-range migration of self-interstitial atoms in tungsten obtained by direct measurement of radiation-induced point-defect clusters, *Philosophical Magazine Letters* 91 (2) (2011) 86–96.

[70] J. Heikinheimo, K. Mizohata, J. Räisänen, T. Ahlgren, P. Jalkanen, A. Lahtinen, N. Catarino, E. Alves, F. Tuomisto, Direct observation of mono-vacancy and self-interstitial recovery in tungsten, *APL Materials* 7 (2).

[71] T. D. Swinburne, P.-W. Ma, S. L. Dudarev, Low temperature diffusivity of self-interstitial defects in tungsten, *New Journal of Physics* 19 (7) (2017) 073024.

[72] J. Mundy, S. Rothman, N. Lam, H. Hoff, L. Nowicki, Self-diffusion in tungsten, *Physical Review B* 18 (12) (1978) 6566.

[73] M. Hossain, J. Marian, Stress-dependent solute energetics in w–re alloys from first-principles calculations, *Acta materialia* 80 (2014) 107–117.

[74] V. Maksimenko, A. Lipnitskii, A. Kartamyshev, D. Poletaev, Y. R. Kolobov, The n-body interatomic potential for molecular dynamics simulations of diffusion in tungsten, *Computational Materials Science* 202 (2022) 110962.

[75] V. Borodin, Rate theory for one-dimensional diffusion, *Physica A: Statistical Mechanics and its Applications* 260 (3-4) (1998) 467–478.

[76] S. Huang, J. Marian, Rates of diffusion controlled reactions for one-dimensionally-moving species in 3d space, *Philosophical Magazine* 99 (20) (2019) 2562–2583.

[77] A. Reza, H. Yu, K. Mizohata, F. Hofmann, Thermal diffusivity degradation and point defect density in self-ion implanted tungsten, *Acta Materialia* 193 (2020) 270–279.

[78] Y. G. Li, W. H. Zhou, R. H. Ning, L. F. Huang, Z. Zeng, X. Ju, A cluster dynamics model for accumulation of helium in tungsten under helium ions and neutron irradiation, *Communications in Computational Physics* 11 (5) (2012) 1547–1568. doi:10.4208/cicp.030311.090611a.

[79] X. Li, Y. Wang, Y. Zhang, Y. Xu, X.-Y. Li, X. Wang, Q. Fang, X. Wu, C. Liu, Towards the dependence of radiation damage on the grain boundary character and grain size in tungsten: A combined study of molecular statics and rate theory, *Journal of Nuclear Materials* 563 (2022) 153637.

[80] T. Hwang, M. Fukuda, S. Nogami, A. Hasegawa, H. Usami, K. Yabuchi, K. Ozawa, H. Tani-gawa, Effect of self-ion irradiation on hardening and microstructure of tungsten, *Nuclear Materials and Energy* 9 (2016) 430 – 435.

[81] A. Debelle, M. Barthe, T. Sauvage, First temperature stage evolution of irradiation-induced defects in tungsten studied by positron annihilation spectroscopy, *Journal of Nuclear Materials* 376 (2) (2008) 216–221.

[82] S. Wang, W. Guo, H. Wang, X. Yi, L. Ge, Y. Sun, L. Cheng, X. Zhang, Y. Yuan, X. Cao, et al., Defect annealing in heavy-ion irradiated tungsten: Long-time thermal evolution of saturated displacement damage at different temperatures, *Journal of Nuclear Materials* 581 (2023) 154454.

[83] S. Hasanzadeh, R. Schäublin, B. Décamps, V. Rousson, E. Autissier, M. F. Barthe, C. Hébert, Three-dimensional scanning transmission electron microscopy of dislocation loops in tungsten, *Micron* 113 (2018) 24–33.

[84] R. Alexander, M.-C. Marinica, L. Proville, F. Willaime, K. Arakawa, M. R. Gilbert, S. L. Dudarev, Ab initio scaling laws for the formation energy of nanosized interstitial defect clusters in iron, tungsten, *Phys. Rev. B* 94 (2016) 024103. doi:10.1103/PhysRevB.94.024103.  
URL <https://link.aps.org/doi/10.1103/PhysRevB.94.024103>

[85] D. R. Mason, D. Nguyen-Manh, M.-C. Marinica, R. Alexander, A. E. Sand, S. L. Dudarev, Relaxation volumes of microscopic and mesoscopic irradiation-induced defects in tungsten, *Journal of Applied Physics* 126 (7).

[86] J. Marian, B. Wirth, R. Schäublin, J. Perlado, T. D. de la Rubia,  $<100>$ -loop characterization in  $\alpha$ -fe: comparison between experiments and modeling, *Journal of nuclear materials* 307 (2002) 871–875.

[87] J. Marian, V. V. Bulatov, Stochastic cluster dynamics method for simulations of multispecies irradiation damage accumulation, *Journal of Nuclear Materials* 415 (1) (2011) 84–95.

[88] J. Marian, T. L. Hoang, Modeling fast neutron irradiation damage accumulation in tungsten, *Journal of Nuclear Materials* 429 (1?3) (2012) 293–297.

[89] A. Dunn, R. Dingreville, E. Martínez, L. Capolungo, Synchronous parallel spatially resolved stochastic cluster dynamics, *Computational Materials Science* 120 (2016) 43 – 52. doi:<https://doi.org/10.1016/j.commatsci.2016.04.013>.  
URL <http://www.sciencedirect.com/science/article/pii/S0927025616301720>

[90] Y. Hu, F. Qian, X. Li, H. Tong, Y. Zhang, Y. Xu, Z. Xie, R. Liu, X.-Y. Li, X. Wu, et al., Helium effect on temperature-displacement rate equivalence in radiation-induced swelling of iron: A study by improved stochastic cluster dynamics, Nuclear Materials and Energy (2025) 101977.

[91] Q. Yu, M. J. Simmonds, R. Doerner, G. R. Tynan, L. Yang, B. D. Wirth, J. Marian, Understanding hydrogen retention in damaged tungsten using experimentally-guided models of complex multispecies evolution, Nuclear Fusion 60 (9) (2020) 096003.

[92] S. He, B. D. Wirth, L. Snead, J. R. Trelewicz, Y. Katoh, S. J. Zinkle, J. Marian, Simulations of radiation damage accumulation in fe-9cr under pulsed irradiation conditions representative of Journal of Nuclear Materials 601 (2024) 155325. doi:<https://doi.org/10.1016/j.jnucmat.2024.155325>. URL <https://www.sciencedirect.com/science/article/pii/S0022311524004276>

[93] M. Norgett, M. Robinson, I. M. Torrens, A proposed method of calculating displacement dose rates, Nuclear engineering and design 33 (1) (1975) 50–54.

[94] S. Zinkle, R. Stoller, Quantifying defect production in solids at finite temperatures: Thermally-activated correlated defect recombination corrections to dpa (crc-dpa), Journal of Nuclear Materials 577 (2023) 154292.

[95] C. Becquart, A. Barbu, J. Bocquet, M. Caturla, C. Domain, C.-C. Fu, S. Golubov, M. Hou, L. Malerba, C. Ortiz, A. Souidi, R. Stoller, Modeling the long-term evolution of the primary damage in ferritic alloys using coarse-grained methods, Journal of Nuclear Materials 406 (1) (2010) 39 – 54, fP6 IP PERFECT Project: Prediction of Irradiation Damage Effects in Reactor Components. doi:<https://doi.org/10.1016/j.jnucmat.2010.05.019>. URL <http://www.sciencedirect.com/science/article/pii/S002231151000231X>